First-principles investigation of the concentration effect on equilibrium fractionation of K isotopes in feldspars

5 authors, including:

Li Yonghui
University of Science and Technology of China
2 PUBLICATIONS **0** CITATIONS

SEE PROFILE

Wenzhong Wang
University of Science and Technology of China
10 PUBLICATIONS **31** CITATIONS

SEE PROFILE

Shichun Huang
University of Nevada, Las Vegas
117 PUBLICATIONS **1,485** CITATIONS

SEE PROFILE

Kun Wang
Washington University in St. Louis
21 PUBLICATIONS **288** CITATIONS

SEE PROFILE

Some of the authors of this publication are also working on these related projects:

Water in the deep mantle View project

Geophysics View project

First-principles investigation of the concentration effect on equilibrium fractionation of K isotopes in feldspars

Yonghui Li [a], Wenzhong Wang [a], Shichun Huang [b], Kun Wang [c], Zhongqing Wu [a,*]

[a] *Laboratory of Seismology and Physics of Earth's Interior, School of Earth and Space Sciences, University of Science and Technology of China, Hefei, Anhui 230026, China*
[b] *Department of Geoscience, University of Nevada, Las Vegas, NV 89154, United States*
[c] *Department of Earth and Planetary Sciences, Washington University in St. Louis, One Brookings Dr. St., Louis, MO 63130, United States*

Abstract

The K concentration effects on K-O bond length and the reduced partition function ratios of $^{41}K/^{39}K$ in alkali feldspars have been explored using the density functional theory (DFT) method. In alkali feldspars, the average K-O bond length increases with increasing K content, measured as $K/(K + Na)$ molar ratio, ranging from 2.724 Å in alkali feldspar with a $K/(K + Na)$ of 1/16 to 2.880 Å in microcline ($K/(K + Na) = 1$). Our results show large K concentration effect on the calculated reduced partition function ratio. For example, $10^3 \ln\,^{41K/39K}\alpha_{feldspar-microcline}$ between alkali feldspar with a $K/(K + Na)$ of 1/16 and microcline are 2.21‰ at 300 K and 0.42‰ at 700 K, which are comparable to the $^{41}K/^{39}K$ variation observed in natural samples. Furthermore, isotope fractionation, $10^3 \ln\,^{41K/39K}\alpha_{feldspar-microcline}$, is negatively linearly correlated with the average K-O bond length in alkali feldspars. Therefore, the concentration effect on K isotope fractionations needs to be considered in the applications of K isotopes in the fields of geochemistry and cosmochemistry, such as the formation of the lunar anorthositic crust and the evolution of the Earth's crust.
© 2018 Elsevier Ltd. All rights reserved.

Keywords: K isotope equilibrium fractionation; First-principles calculation; Concentration effects

1. INTRODUCTION

Potassium (K) is an alkalic, large-ion lithophile and moderately volatile element, with a 50% condensation temperature of 1006 K in a solar composition gas at 10^{-4} bar total pressure, similar to those of Zn, Na, Rb and Cs (Lodders, 2003). K has three naturally occurring isotopes: ^{39}K (93.2581%), ^{40}K (0.0117%) and ^{41}K (6.7302%). ^{40}K is radioactive ($t_{1/2} = 1.250 \times 10^9$ years) with two decay products: β^+ decay to ^{40}Ar (11.2%), and β^- decay to ^{40}Ca (88.8%). The ^{40}K-^{40}Ar system is widely used in the field of geochronology. In recent years, the K stable isotope compositions, usually reported as $\delta^{41}K_{Standard}$ ($\delta^{41}K_{Standard} = \left[\left(\left(^{41}K/^{39}K\right)_{Sample}/\left(^{41}K/^{39}K\right)_{Standard}\right) - 1\right] \times 1000$), become an important cosmochemical and geochemical tracer (e.g., Humayun and Clayton, 1995a, 1995b; Humayun and Koeberl, 2004; Wang and Jacobsen, 2016a, 2016b; Parendo et al., 2017; Bloom et al., 2018; Chen et al., 2018a, 2018b; Hu et al., 2018; Jiang et al., 2018; Lee et al., 2018; Morgan et al., 2018; Santiago Ramos et al., 2018; Tian et al., 2018a, 2018b; Tuller-Ross et al., 2018).

K isotope fractionation has been used to study the origin of volatile element depletion in rocky planets. At ±0.5‰ level, Humayun and Clayton (1995a) showed that all differentiated and undifferentiated meteorites have essentially the same $\delta^{41}K$, regardless of their variable degrees of K

---

depletion. This result is inconsistent with K loss via a Rayleigh evaporation process, i.e., evaporation under vacuum, which predicts that the Earth and the Moon have much higher $\delta^{41}K$, by several percent, than chondrites. Recently, using Multi-Collector Inductively Coupled Plasma Mass-Spectrometer (MC-ICP-MS), high precision K isotope measurement at the level of $\pm0.05‰$ for $\delta^{41}K$ is now possible (Wang and Jacobsen, 2016a; Li et al., 2016; Hu et al., 2018; Morgan et al., 2018). With such high precision, Wang and Jacobsen (2016a) reported that lunar basalts have $\delta^{41}K$ 0.4‰ higher than the Earth, a small but important difference that could not be resolved in the 1990s (Humayun and Clayton, 1995a). This Earth-Moon K isotope difference is still too small to be explained by a Rayleigh evaporation process in the vacuum for the K depletion of the Moon. However, the correlation between K depletion and K isotope fractionation between the Earth and Moon can be explained if K was lost during evaporation under pressure or if K partially condensed from a Bulk Silicate Earth (BSE) vapor during Moon formation (Wang and Jacobsen, 2016a). This is because isotope fractionation during evaporation under pressure is usually suppressed with an effective fractionation factor increasing from 0.975 at around 10^{-9} bar to 0.999 at 1 bar, i.e., less isotope fractionation under higher pressure (Humayun and Cassen, 2000; Yu et al., 2003; Richter et al., 2011; Wang and Jacobsen, 2016b).

Large $\delta^{41}K$ variations have been observed in both lunar and terrestrial igneous rocks. For example, Humayun and Clayton (1995b) reported extremely low $\delta^{41}K_{BSE}$ value ($-3.40 \pm 0.94‰$) for lunar anorthosite 60015, which is confirmed by more recent study on lunar anorthosites (Tian et al., 2018b). The light K isotope composition of lunar anorthosites are very different from the bulk Moon $\delta^{41}K_{BSE}$ estimate ($+0.44 \pm 0.16‰$) of Wang and Jacobsen (2016b) based on the measurements of 7 lunar basalts/highland rocks. It appears that there is large (several per mil) K isotope fractionation between lunar basalts and anorthosites. The mechanism of such fractionation is still not understood. Among terrestrial samples, Morgan et al. (2018) also found large $\delta^{41}K_{BSE}$ variation, $-0.71‰$ to 0.16‰, in terrestrial feldspar samples. Those findings imply possible K isotope fractionation during igneous processes, including crystal fractionation. Consequently, knowledge of K isotope fractionation during igneous processes is required for a more thorough understanding of the reported $\delta^{41}K$ difference between the Earth and Moon.

The K isotope fractionation factors among K-bearing minerals and between minerals and melt are critical for understanding the K isotope compositions of the lower continental and oceanic crusts, which are rich in plagioclase and play an important role in continental crust formation (e.g., Jagoutz and Behn, 2013; Gazel et al., 2015; Kelemen and Behn, 2016; Tamura et al., 2016), and generating mantle heterogeneity (e.g., Hofmann and Jochun, 1996; Sobolev et al., 2000; Chauvel and Hemond, 2000; Yang et al., 2003; Saal et al., 2007; Peterson et al., 2014; Frey et al., 2016; Huang and Humayun, 2016).

Inter-mineral and mineral-magma K isotope fractionation factors are also important to the fields of cosmochem-

istry and geochemistry; however, direct measurements of such factors are not available. First-principles calculations based on the density functional theory (DFT) have successfully predicted equilibrium inter-mineral isotope fractionation factors of many important rock-forming element including Mg, Ca and Si (e.g., Feng et al., 2014; Huang et al., 2014; Wu et al., 2015; Qin et al., 2016; Wang et al., 2017a, 2017b). Since alkali feldspars ($(K, Na)AlSi_3O_8$) are the major K-bearing minerals in the crust (Anderson and Anderson, 2010), we present the reduced partition function ratios of alkali feldspars using first-principles calculations, which can be used in the future to better constrain the mineral-magma and magma-gas isotope fractionation factors of K isotopes.

2. METHODS

In a harmonic approximation, the reduced partition function ratio β_A of element X in phase A, which is the ratio of the isotope compositions of element X between phase A and an ideal mono-atomic gas, can be expressed by

$$\beta_A = \prod_i^{3N-3} \frac{u_{ih}}{u_{il}} \frac{e^{-\frac{1}{2}u_{ih}}}{(1-e^{-u_{ih}})} \frac{(1-e^{-u_{il}})}{e^{-\frac{1}{2}u_{il}}}. \qquad (1)$$

where h and l represent the heavy and light isotopes, respectively; i is the index of vibration modes which varies from 1 to $3N-3$ for a crystal with N atoms. u_i is defined as

$$u_i = \frac{h\nu_i}{kT}. \qquad (2)$$

where h is the Planck constant, ν_i is the vibrational frequency of the ith mode, k is the Boltzmann constant, and T is temperature in Kelvin. The equilibrium isotope fractionation factor of element X between phase A and B, $\alpha_{A-B} = \beta_A/\beta_B$, is expressed by

$$\Delta_{A-B} = 10^3 \ln \alpha_{A-B} = 10^3 (\ln \beta_A - \ln \beta_B). \qquad (3)$$

The Quantum Espresso software package, based on DFT, plane-wave basis set, and pseudopotentials (Giannozzi et al., 2009), is used to optimize the mineral structures discussed in this paper and to calculate their vibration frequencies. Local density approximation (LDA) is adopted to describe the exchange–correlation energy (Perdew and Zunger, 1981), and the energy cut-off for plane waves is 70 Rydberg.

The Na and K pseudopotentials were generated by Giannozzi using Von Barth and Car method in 1993 (unpublished method, for a brief description of this method, see Dal Corso et al., 1993), using valence electron configurations of $3s^1$ and $4s^1$, respectively. The pseudopotentials of Si and O are adopted from our previous studies (Feng et al., 2014; Huang et al., 2014; Wu et al., 2015; Qin et al., 2016; Wang et al., 2017a, 2017b), which were generated using the method of Troullier and Martins (1991) with valence electron configurations of $3s^2 3p^4 3d^0$ and 1.47 Bohr cutoff radius for Si, $2s^2 2p^4$ and 1.45 cutoff radius for O. The Al pseudopotential is generated following Vanderbilt (1990), with a valence electron configuration of $3s^2 3p^1$ and 1.77 Bohr cutoff radius (Hu et al., 2016).

The alkali feldspars are solid solution series of two end-members: albite ($NaAlSi_3O_8$) and K-feldspar ($KAlSi_3O_8$). The Na-endmember can be divided into high albite (anal-bite) and low albite based on the Al-Si ordering in the tetra-hedral sites with a transformation temperature near 1020 K (Parsons, 1978, 2010; Smith and Brown, 1988; Meneghinello et al., 1999; Parsons and Lee, 2009; Norberg et al., 2011; Parsons et al., 2015). Both low and high albites are triclinic with four non-equivalent tetrahe-dral sites, T1m, T1o, T2m and T2o (Fig. S2), occupied by Al and Si atoms. Low albite has the highest Al-Si ordering with T1o site being completely occupied by Al. In high albite, Al occupies both T1o and T1m sites. At higher tem-perature (above 1320 K), the albite crystal symmetry changes from triclinic to monoclinic with complete Al-Si disordering (Parsons, 1978, 2010; Smith and Brown, 1988; Parsons et al., 2015) to form monalbite.

Microcline is the most stable form of K-feldspar at low temperature. It has a triclinic symmetry, with T1o site being completely occupied by Al, i.e., the highest Al-Si ordering. With increasing temperature, the Al-Si ordering is gradu-ally destroyed, and at 770 K, it turns to monoclinic sanidine with complete Al-Si disordering. However, the reverse tran-sition does not occur naturally. With decreasing tempera-ture, the change of sanidine to microcline has never been achieved in experiments (Parsons et al., 2015), because the Al-Si re-ordering is prohibited by the formation of the anti-phase domains (Parsons, 1978, 2010; Smith and Brown, 1988; Meneghinello et al., 1999; Parsons et al., 2015). Instead, four different orientated unit cells nucleate to form monoclinic orthoclase, which is a metastable form and transforms to microcline during coarsening domain evolu-tion such as dissolution-reprecipitation reaction (Lee et al., 1995) and retrograde reactions (Waldron et al., 1993).

The initial low albite and microcline structures were taken from Prewitt et al. (1976) and Chao et al. (1940), respectively. Low albite and microcline with C-1 space group have four symmetrically equivalent alkali atom sites in a 52-atom unit cell. By replacing Na atoms with K atoms in albite or K atoms with Na atoms in microcline, we generated the initial feldspar structures with various $K/(K + Na)$. For example, one of the 16 Na atoms in a 208-atom super cell of albite was substituted by one K atom to make a feldspar with a $K/(K + Na)$ of 1/16. There are multiples occupancy configurations for feldspar structures with $K/(K + Na)$ of 2/8, 2/4 and 5/8. We searched all nonequivalent occupancy configurations using a 104-atom cell for $K/(K + Na)$ of 2/8 and 5/8 (6 and 7 configurations respectively), and a 52-atom cell for a $K/(K + Na)$ of 2/4 (3 configurations). Then, those initial structures were opti-mized using variable cell shape molecular dynamics (Wentzcovitch, 1991) with force, stress and self-consistency energy convergence set at 10^{-4} Ry/Bohr, 0.5 Kbar and 10^{-8} Ry, respectively. The Wentzcovitch (1991)'s extended lagrangian calculation was applied in the cell dynamics. The k points sampling in the Brillouin zone was set according to the crystal cell size (Fig. 1). We used a $1 \times 2 \times 1\, k$ mesh for the 208-atoms super cell of feldspar with a $K/(K + Na)$ of 1/16, and a $2 \times 2 \times 2\, k$ mesh for others. In order to test the convergence of the k mesh,

we also optimized microcline using a $4 \times 4 \times 4\, k$ mesh. The optimized structure parameters (Table 1) and average K-O bond lengths (Table 2) agree well with the results opti-mized using a $2 \times 2 \times 2\, k$ mesh. Then we chose the config-urations with the lowest total energy for the vibration frequency calculation. The vibrational frequencies were computed using density-functional perturbation theory (DFPT) on the gamma point with self-consistency thresh-old set at 10^{-14} and the Acoustic Sum Rule (ASR) set simple. We also conducted vibrational calculations using 4 q-points in microcline, which has the smallest cell among all structures. As shown in Section 3.3, the results from cal-culations using the gamma-point only are comparable to those from calculations using 4 q-points.

3. RESULTS

3.1. Crystal structures

The optimized feldspar structures are shown in Fig. 1. The optimized structure parameters of low albite and microcline (Table 1) agree well with the X-ray diffraction measurements on natural samples (Blasi et al., 1987; Downs et al., 1994; Makreski et al., 2009). Our calculations reproduce the dependence of feldspar volumes on their K contents (Fig. 2), and the vibration frequencies of low albite and microcline (Fig. 3). Specifically, our calculated vibra-tion frequencies and experimental Raman and Infrared Radiation (IR) data plot on a 1:1 line (slope = 1.00 ± 0.01, 1σ, $R^2 = 0.99987$) (Fig. 3). As shown in previous studies (Huang et al., 2013; Feng et al., 2014; Wu et al., 2015; Hu et al., 2016; Wang et al., 2017a, 2017b), the LDA is a good exchange correlation functional for calculat-ing isotope fractionation among minerals. According to the error analyses of Méheut et al. (2009), a relative uncertainty of the calculated frequencies of n% will result in an uncer-tainty of n% at low temperature and $2n$% at high tempera-ture, respectively, for the calculated reduced partition function ratio $10^3 \ln \beta$. Our calculated frequencies scaling factor is 1.00 ± 0.01 (1σ), with an uncertainty of 1%. Thus, under the temperature interval discussed in this paper, 700–1000 K, the relative uncertainties of our calculated $10^3 \ln \beta$ and $10^3 \ln \alpha$ are 2% and 3%, respectively.

3.2. KO bond lengths in feldspars

Based on electron-density distribution, Downs et al. (1996) suggested that the coordination number (CN) of alkali cation is 5 and 7 in albite and microcline, respectively. The average K—O bond lengths with CN = 5, 6 and 7 are illustrated in Fig. 4. We reach similar relationships between the average K—O bond lengths and $K/(K + Na)$ for CN = 5, 6 and 7 (Fig. 4), which show that the K content effect on the average bond length is insensitive to which CN is used. In this work, we chose a CN of 5. The averages of the five shortest K—O bonds for all of structures are shown in Table 2, Fig. 4.

Because K^+ is much larger than Na^+, NaO_5 polyhedron in low albite is smaller than KO_5 polyhedron in microcline. Consequently, we expect a shorter K—O bond in low albite
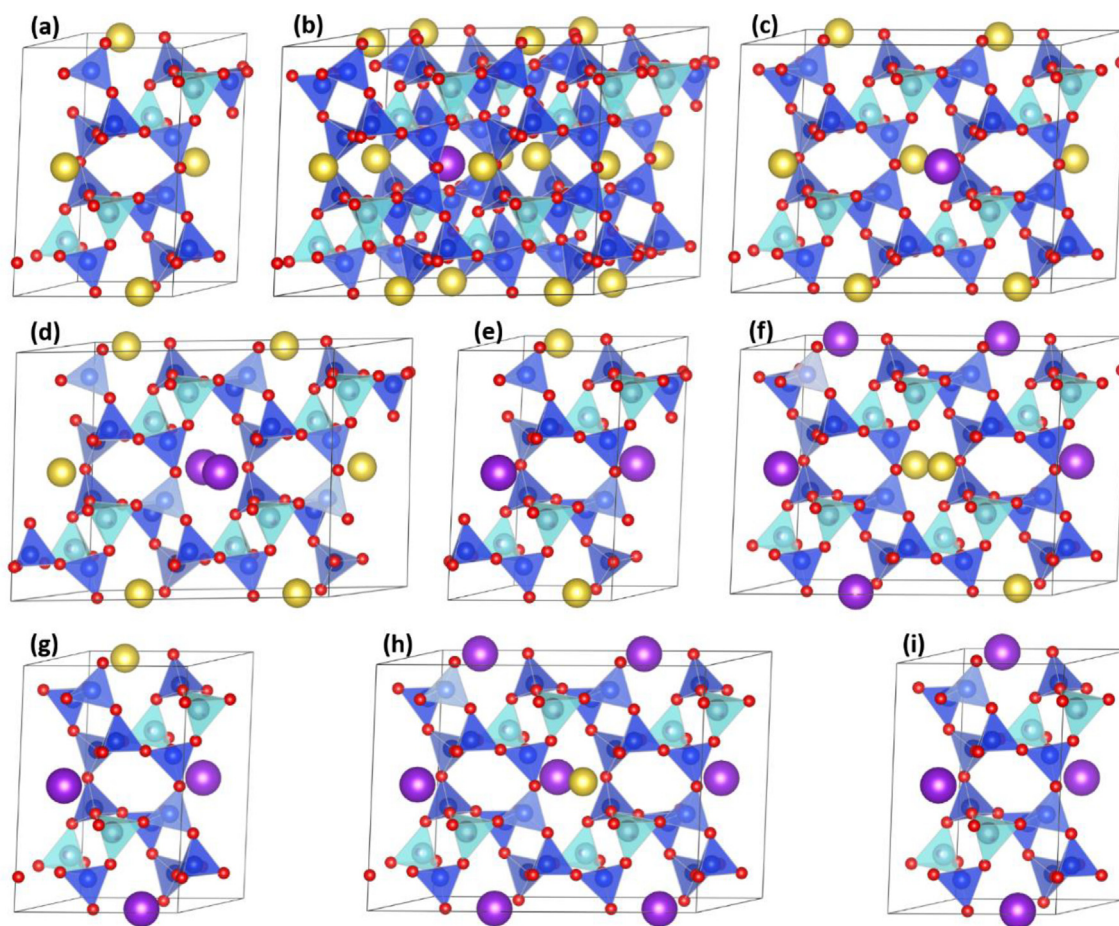
Fig. 1. Structures of alkali feldspars with different K/(K + Na) (a) 0 (low albite), (b) 1/16 (0.0625), (c) 1/8 (0.125), (d) 2/8 (0.25), (e) 2/4 (0.5), (f) 5/8 (0.625), (g) 3/4 (0.75), (h) 7/8 (0.875), and (i) 4/4 (1, microcline). Red, O; blue, Si; light cyan, Al; purple, K; yellow, Na. All are low temperature structures with all Al atoms occupying T1o sites. The albite and microcline structures are from American Mineralogist Crystal Structure Database (http://rruff.geo.arizona.edu/AMS/amcsd.php). (For interpretation of the references to color in this figure legend, the reader is referred to the web version of this article.)

Table 1
The relaxed structure parameters at static conditions compared with experimental data at 1 atm, room temperature.

Minerals	a/Å	b	c	α/°	β	γ	V/Å^3	
KAlSi$_3$O$_8$	8.447	12.954	7.214	90.75	114.24	91.74	719.16	Exp. 1
	8.571	12.964	7.221	90.64	115.95	87.68	720.99	Exp. 2
	8.600	12.942	7.199	90.48	116.30	87.96	717.79	This study
	8.599	12.946	7.199	90.49	116.35	87.92	717.64	This study*
NaAlSi$_3$O$_8$	8.074	12.773	7.153	94.27	115.80	88.53	662.27	Exp. 1
	8.137	12.787	7.157	94.25	116.61	87.81	664.02	Exp. 3
	8.193	12.816	7.167	93.05	116.76	87.72	670.75	This study

Data sources: Exp. 1, Makreski et al. (2009) powder X-ray diffraction data; Exp. 2, Blasi et al. (1987) single-crystal X-ray diffraction data; Exp. 3, Downs et al. (1994) single-crystal X-ray diffraction data.
This study * represents the microcline structure parameters optimized using a 4 × 4 × 4 k mesh.

than that in microcline. As shown in Fig. 4 and Table 2, the average K—O bond length increases with increasing K/(K + Na). Among all explored compositions in this study, the alkali feldspar with a K/(K + Na) of 1/16 has the shortest

average K—O bond length of 2.724 Å, and microcline (pure K-feldspar, K/(K + Na) = 1) has the longest average K—O bond length of 2.880 Å, which agrees with the X-ray diffraction data (Blasi et al., 1987) within 0.5% (Table 2).

Table 2
Average of the shortest five K-O bond lengths of alkali feldspars at static conditions compared with the experiment data at 1 atm, room temperature.

Minerals	K/(K + Na)	Average K-O bond length (Å)	
		This study	Blasi et al. (1987)
Alkali feldspar	0		
	1/16	2.724	
	1/8	2.742	
	2/8	2.779	
	2/2	2.804	
	5/8	2.837	
	3/4	2.844	
	7/8	2.862	
Microcline	4/4	2.880	2.864
Microcline*	4/4	2.880	

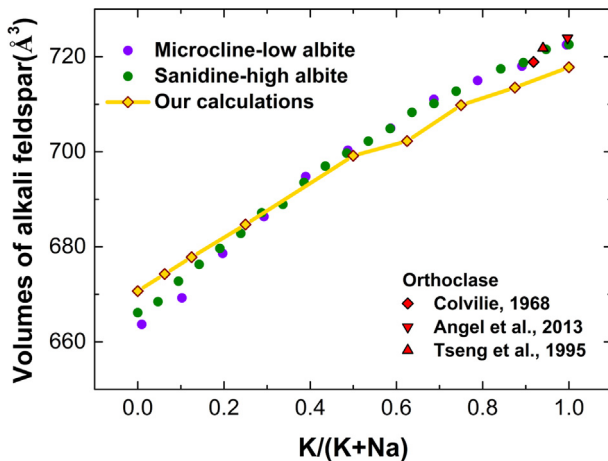Microcline* represents the microcline structure optimized using a $4 \times 4 \times 4\,k$ mesh.

Fig. 2. The measured volumes of alkali feldspars versus K/(K + Na). Our calculations reproduce the measurements of microcline-low albite and sanidine-high albite solid solution series (Orvilie, 1967) and orthoclases (Colvilie, 1968; Tseng et al., 1995; Angel et al., 2013). Details with standard errors are in Table S1.

3.3. K isotope fractionation

The calculated reduced partition function ratios, $10^3 \ln {}^{41K/39K}\beta$, of alkali feldspars as a function of K/(K + Na) and temperature are shown in Fig. 5, and the equilibrium isotope fractionation factors, $10^3 \ln {}^{41K/39K}\alpha_{feldspar-microcline}$, are shown in Fig. 6. Their polynomial fitting parameters are listed in Table 3.

As shown in Fig. 5, $10^3 \ln {}^{41K/39K}\beta$ decreases with increasing K/(K + Na) in alkali feldspar. The alkali feldspar with a K/(K + Na) of 1/16 has the shortest average K—O bond length and the largest $10^3 \ln {}^{41K/39K}\beta$ among all calculated alkali feldspars in this study. Microcline has the longest average K—O bond length, and consequently, the smallest $10^3 \ln {}^{41K/39K}\beta$ among all alkali feldspars. This tendency is
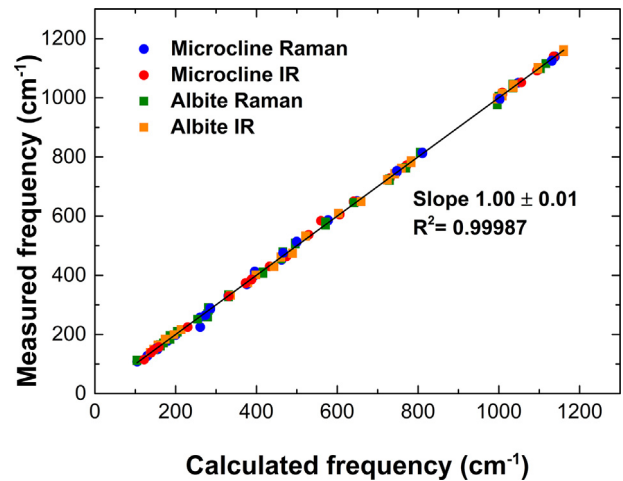

Fig. 3. Calculated vibrational frequencies of microcline and low albite compared with the experimental Raman and IR data: Raman data: Velde et al. (1989), McKeown (2005), Makreski et al. (2009), Sharma et al. (2010) for albite. Velde and Boyer (1985), Villar and Edwards (2005), Makreski et al. (2009), Sharma et al. (2010) for microcline. IR data: Moenke (1962), Couty and Velde (1986), Makreski et al. (2009) for albite. Moenke (1962), Handke and Mozgawa (1993), Makreski et al. (2009) for microcline.
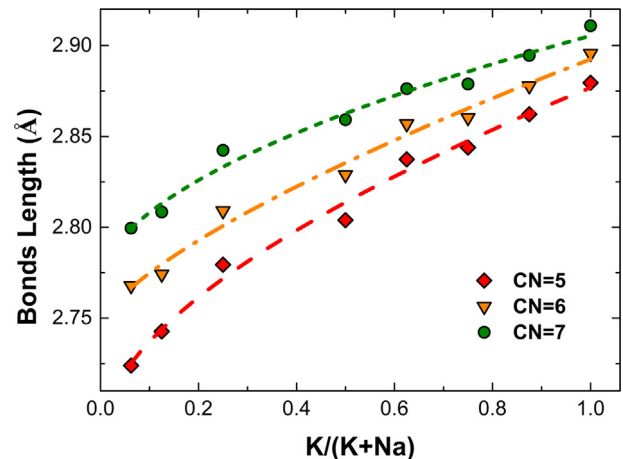

Fig. 4. The average of the 5, 6 and 7 shortest K-O bond length versus K/(K + Na) of alkali feldspars. The dash, dash-dot and short dash lines are nonlinear fitting curves with R^2 of 0.99, 0.98 and 0.97 respectively.

similar to the published Mg isotope studies in carbonates and Ca isotope studies in orthopyroxene (Feng et al., 2014; Wang et al., 2017a, 2017b).

Using the generalized gradient approximation (GGA) for the exchange-correlation energy, Zeng et al. (2018) predicted a much larger volume (5.6%) and a much smaller $10^3 \ln {}^{41K/39K}\beta$ (−48.2%) for microcline than our calculations based on LDA. $10^3 \ln {}^{41K/39K}\beta$ is sensitive to the K—O bond length and, hence, the volume of microcline. We explore this relationship by checking the pressure effect on K—O bond length, volume, and $10^3 \ln {}^{41K/39K}\beta$ of microcline.
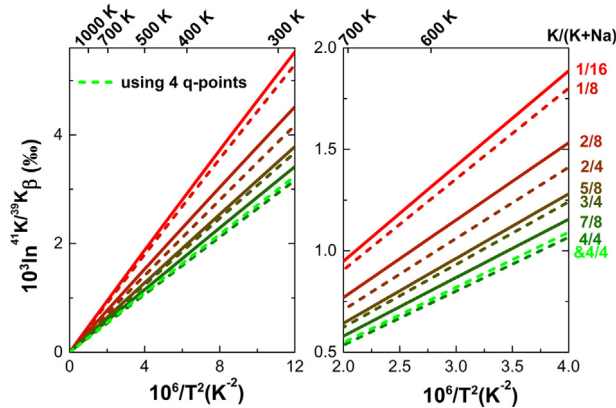
Fig. 5. Reduced partition function ratio ($10^3 \ln {}^{41K/39K}\beta$) of eight feldspar structures as a function of temperature. Their K/(K + Na) are labeled at the right end of the lines. The reduced partition function ratio of microcline (K/(K + Na) = 4/4) calculated using 4 q-points (the green short dash line) is very close to the results calculated using only gama point (the olive short dash line). (For interpretation of the references to color in this figure legend, the reader is referred to the web version of this article.)
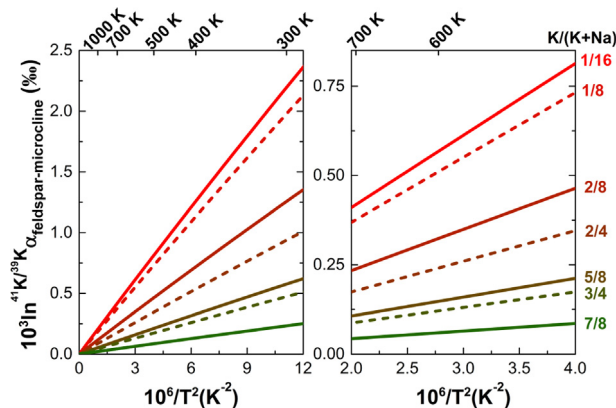

Fig. 6. Equilibrium K isotope fractionation factors between feldspars and microcline, $10^3 \ln {}^{41K/39K}\alpha_{feldspar-microcline} = 10^3 \left(\ln {}^{41K/39K}\beta_{feldspar} - \ln {}^{41K/39K}\beta_{microcline} \right)$. Their K/(K + Na) are shown at the right end of the lines.

Our calculations indicate that $10^3 \ln {}^{41K/39K}\beta$ increases by 13.7%, and the volume decreases by 1.5% from 0 GPa to 1 GPa. Consequently, the smaller $10^3 \ln {}^{41K/39K}\beta$ of microcline obtained by Zeng et al. (2018) is consistent with their larger volume. Because of the much larger static volume predicted by GGA, ~5% larger than experiment data (Zeng et al., 2018), it is more appropriate to use LDA for alkali feldspar calculation.

The equilibrium K isotope fractionation factors between alkali feldspars and microcline vary with K/(K + Na) in alkali feldspars (Fig. 7). The K content in feldspar is another important factor besides temperature that controls the equilibrium K isotope fractionation factor between feldspars. The largest $10^3 \ln {}^{41K/39K}\alpha_{feldspar-microcline}$ in this study

occurs between alkali feldspar with a K/(K + Na) of 1/16 and microcline, 2.21‰ at 300 K and 0.42‰ at 700 K, respectively. These values are comparable to the $\delta^{41}K_{BSE}$ variations found in terrestrial silicate rocks, which range from −0.88 ± 0.34‰ to 0.49 ± 0.17‰ (Wang and Jacobsen, 2016a, 2016b; Li et al., 2016; Morgan et al., 2018).

4. DISCUSSIONS

4.1. Concentration effects in alkali feldspars

Feng et al. (2014) and Wang et al. (2017a, 2017b) demonstrated that Ca concentrations in orthopyroxene and carbonate minerals (calcite, dolomite, and aragonite) affect their mineral Ca-O bond lengths, and that the radius difference between Ca^{2+} and Mg^{2+} is crucial for the concentration effect on the bond lengths. In a mineral with its cation site dominated by B cations, when a small amount of A cations replace B cations, A cations should fit into the mineral structure controlled by B cations. When A cations are dominant in the mineral, A cations will adopt a structure controlled by A cations. Thus, the effect from B cations decreases with increasing the concentration of A cations, which causes the concentration dependence of the A—O bond lengths.

Furthermore, comparison of our study with previous studies (Feng et al., 2014; Wang et al., 2017a, 2017b) yields a better understanding of the importance of the cation size difference to the concentration effect. Radius difference between K^+ (1.520 Å) and Na^+ (1.160 Å) is larger than that between Ca^{2+} (1.140 Å) and Mg^{2+} (0.860 Å) (Shannon, 1976). As a consequence, K—O bond in microcline (2.864 Å) (Blasi et al., 1987) is 15% longer than Na—O bond in albite (2.494 Å) (Downs et al., 1994), while Ca—O bond in calcite (2.360 Å) is only ~12% longer than Mg—O bond in magnesite (2.102 Å). Correspondingly, average K—O bond length increases about ~6% from 2.724 Å in alkali feldspar with a K/(K + Na) of 1/16 to 2.880 Å in microcline, while average Ca—O bond length only increases about 3% from 2.273 Å in magnesite with a Ca/(Mg + Ca) of 1/36 to 2.341 Å in pure calcite.

As shown in previous studies (Urey, 1947; Schauble et al., 2004; Feng et al., 2014; Qin et al., 2016; Wang et al., 2017a, 2017b), a longer bond corresponds to a weaker bond strength and a lower vibrational frequency, and results in enrichment in lighter isotopes relative to a shorter and stronger bond. Alkali feldspars with low K/(K + Na) have shorter K—O bonds and larger $10^3 \ln {}^{41K/39K}\alpha_{feldspar-microcline}$, resulting in a negative correlation between the average K—O bond length and $10^3 \ln {}^{41K/39K}\alpha_{feldspar-microcline}$ (Fig. 8). This mimics the behaviors of Ca isotopes in orthopyroxene (Feng et al., 2014; Wang et al., 2017b) and carbonate minerals (Wang et al., 2017a), which have the similar negative linear relation between the average Ca—O bond length and inter-mineral Ca isotope fractionation factor. The concentration effect on inter-mineral isotope equilibrium fractionation is likely a ubiquitous phenomenon.

Table 3
Polynomial fitting parameters of reduced partition function ratio ($10^3 \ln {}^{41K/39K}\beta$) and equilibrium K isotope fractionation factor between feldspars and microcline ($10^3 \ln {}^{41K/39K}\alpha_{feldspar-microcline}$).

	K/(K + Na)	A	B	C
$10^3 \ln {}^{41K/39K}\beta$	1/16	0.4751	−0.0014	9.80E−06
	1/8	0.4541	−0.0012	8.54E−06
	2/8	0.3860	−0.0009	6.61E−06
	2/4	0.3558	−0.0007	5.38E−06
	5/8	0.3219	−0.0006	4.95E−06
	3/4	0.3122	−0.0006	4.44E−06
	7/8	0.2900	−0.0005	4.52E−06
	4/4	0.2682	−0.0004	3.95E−06
$10^3 \ln {}^{41K/39K}\alpha_{feldspar-microcline}$	1/16	0.2069	−0.0009	5.87E−06
	1/8	0.1859	−0.0008	4.59E−06
	2/8	0.1178	−0.0004	2.67E−06
	2/4	0.0876	−0.0003	1.44E−06
	5/8	0.0537	−0.0002	9.92E−07
	3/4	0.0440	−0.0001	5.10E−07
	7/8	0.0218	−0.0001	5.79E−07

$10^3 \ln {}^{41K/39K}\alpha_{feldspar-microcline}$, $10^3 \ln {}^{41K/39K}\beta = Ax + Bx^2 + Cx^3$, where x is $10^6/T^2$, T is the temperature in Kelvin. The data used for polynomial fitting are between 553 K and 1673 K.
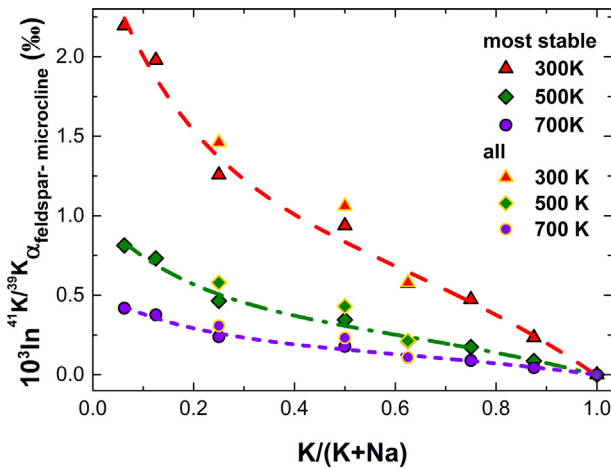

Fig. 7. The dependence of $10^3 \ln {}^{41K/39K}\alpha_{feldspar-microcline}$ on K/(K + Na) at various temperatures. The dash, dash-dot and short-dash lines are nonlinear fitting curves of the "most stable" data with R^2 0.98. The "all" means the estimated $10^3\ln\alpha$ considering the contributions of all the other configurations as discussed in Section 4.1.

Fig. 8. The negative correlation between the equilibrium K isotope fractionation factor $10^3 \ln {}^{41K/39K}\alpha_{feldspar-microcline}$ and the average K-O bond length in feldspars at 300 K, 500 K and 700 K. The dash, dash-dot and short-dash lines are fitting lines with $R^2 > 0.996$.

The concentration effect is more significant at low K/(K + Na) ratio. $10^3 \ln {}^{41K/39K}\alpha_{feldspar-microcline}$ between alkali feldspar with a K/(K + Na) of 1/16 and microcline is 2.21‰ at 300 K and 0.42‰ at 700 K, which are comparable to or larger than K isotope variation in many terrestrial basalts rocks, which range from −0.88 to 0.49, and extraterrestrial samples such as martian meteorites ($\delta^{41}K_{BSE} = +0.12 \pm 0.12$‰) and lunar mare basalts ($\delta^{41}K_{BSE} = +0.44 \pm 0.16$‰) (Wang and Jacobsen, 2016a, 2016b; Tian et al., 2018a, 2018b; Morgan et al., 2018). Therefore, K content is an important factor controlling K isotope fractionation; however, this effect was ignored in previous studies. The
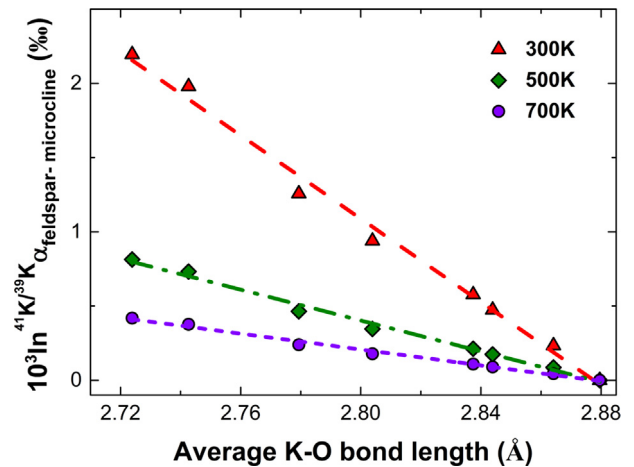
concentration effects on K isotopes fractionation needs to be considered seriously when we use K isotope to trace geological and cosmochemical processes.

K can occupy several cation sites with different configurations in feldspars. In our approach, only the configuration with the lowest energy is considered. The contribution of the other configurations to $10^3\ln\alpha$ can be estimated based on the energy and the structure of the configuration using the Boltzmann distribution and the relationship between $10^3 \ln {}^{41K/39K}\alpha_{feldspar-microcline}$ and average K—O bond length. As shown in Fig. 7, addition of high energy configurations only slightly modifies the $10^3\ln\alpha$. For example, at 700 K the $10^3 \ln {}^{41K/39K}\alpha_{feldspar-microcline}$ between the alkali feldspar with a K/(K + Na) of 0.25

and microcline changes from 0.24‰ to 0.31‰. The concentration effect on K isotope fractionation is nearly proportional to the volume variation caused by K doping. Our calculations underestimate the volume difference between albite and microcline (Fig. 2) and hence underestimate the concentration effect on K isotope fractionation. The $10^3 \ln \alpha$ between alkali feldspar with a K/(K + Na) of 0.0625 and microcline at 300 K (700 K) is underestimated by ~0.50‰ (0.10‰) in our approach.

4.2. Implications for the interpretations of K isotope compositions in natural samples

$10^3 \ln {}^{41K/39K}\alpha_{feldspar-microcline}$ between alkali feldspar with a K/(K + Na) of 1/16 and microcline is 0.42‰ at 700 K, and a lower K/(K + Na) probably leads to a larger fractionation. Low albite usually has a K/(K + Na) less than 1/16 (Harlow and Brown, 1980; Smith and Brown, 1988; Armbruster et al., 1990; Fedo et al., 1997; Spötl et al., 1999; Zhou et al., 2013). Thus our calculations suggest that low albites are significantly enriched in heavy K isotopes relative to microcline. At higher temperature, K/(K + Na) in feldspars vary from 0 to 1 (Fig. 2) in the solid solution series of orthoclase-high albite and sanidine-high albite (Orvilie, 1967; Phillips and Ribbe, 1973; Powell and Powell, 1977; Keefer and Brown, 1978; Lee and Parsons, 1995; White et al., 2003), which in turn lead to large variations in their corresponding reduced partition function ratios, $10^3 \ln {}^{41K/39K}\beta$. The concentration effects on K equilibrium isotope fractionation obtained in this study (low temperature phases) can be applied to future K isotope studies of these solid solution series (high temperature phases).

Orthoclase and sanidine, the high temperature phases of K-feldspar, and microcline, the low temperature phase of K-feldspar, have similar structures, volumes, and K—O bonding environments (Figs. 2, S1–S2) (Orvilie, 1967), and so do high albite and low albite (Fig. 2, S3–S4) (Orvilie, 1967). More importantly, the sanidine-high albite solution series have a volume dependence on K content almost identical to that of the microcline-low albite solution series (Fig. 2), which implies that the sanidine-high albite solution series and microcline-low albite solution series show similar dependence of K—O bond length on K content. Therefore, we expect a significant K concentration effect on K isotope fractionation in the high temperature phase solution series of alkali feldspars. Compared to K-feldspar series, plagioclases, a solid solution series between albite and anorthite, probably are also enriched in heavy K isotopes because of their low K/(K + Na + Ca) and the similar ionic radii of Na and Ca.

Morgan et al. (2018) found large $\delta^{41}K_{BSE}$ variation in terrestrial K-feldspars and K-feldspar-bearing rocks (−0.71‰ to 0.16‰). Among the igneous samples studied, an anorthoclase (an intermediate member of sanidine-high albite solid solution series stable at 873 K and above with a K/(K + Na) of 10–36%), HUG709-K50, has a $\delta^{41}K_{BSE}$ of 0.08‰, and four sanidines from three locations have $\delta^{41}K_{BSE}$ ranging from −0.03‰ to 0.04‰. Among pegmatite minerals, four K-feldspars from four locations have $\delta^{41}K_{BSE}$ ranging from −0.17‰ to 0.16‰. By contrast, six subsamples drilled from a single amazonite crystal, a variety of microcline, from M11650, an A-type granite from Pikes Peak batholith, have $\delta^{41}K_{BSE}$ ranging from −0.71‰ to −0.41‰. Morgan et al. (2018) speculated that some of the $\delta^{41}K_{BSE}$ variation might reflect K isotope fractionation caused by chemical or thermal diffusion, and between silicate and hydrous-halide melt. In addition, K content effects on K isotope fractionation (Figs. 6 and 8) should also contribute to some of the observed variation (Morgan et al., 2018). For comparison, our calculations show that the difference of $\delta^{41}K$ between albite with a K/(K + Na) of 1/16 and microcline is 0.42‰ at 700 K and 0.21‰ at 1000 K. However, compositional data of those feldspar minerals are not available (Morgan et al., 2018).

The lunar anorthosite 60015 is a plagioclase-rich cumulate, and has a very low $\delta^{41}K_{BSE}$ of −3.4‰, which is significantly lower than lunar basalts and other lunar highland rocks (Humayun and Clayton, 1995a; Wang and Jacobsen, 2016a). Tian et al. (2018b) recently confirmed such low $\delta^{41}K_{BSE}$ values in lunar anorthosites. Lunar anorthosites are early cumulates from lunar magma ocean crystallization, and their K isotope compositions are dependent on the mineral-*melt* isotope fractionation factors, which are still unknown. The equilibrium isotope fractionations factors between feldspars calculated in this study cannot be directly applied in the lunar anorthosite case. Humayun and Clayton (1995a) explained this extremely light K as the result of a kinetic isotopic fractionation via the "deposition of (isotopically light) vapor produced by breccia-forming impacts". Such a kinetic explanation is more likely than an equilibrium one due to the large degree of isotope fractionation observed in lunar anorthosites.

5. CONCLUSIONS

The crystal structures and K—O bond lengths of the microcline-low albite solid solution series are calculated using DFT method. The average K—O bond length increases with increasing K/(K + Na) in alkali feldspars. For example, the average K—O bond length increases by 5.7% from alkali feldspar with a K/(K + Na) of 1/16 to microcline (K/(K + Na) = 1), showing great effect of K/(K + Na) on the K—O bonds in microcline-low albite solid solution series. Reduced partition function ratios, $10^3 \ln {}^{41K/39K}\beta$, in alkali feldspars are negatively, linearly correlated with the average K—O bond lengths, similar to Ca reduced partition function ratios in orthopyroxene (Feng et al., 2014; Wang et al., 2017b) and carbonates (Wang et al., 2017a). Hence, the concentration effects on reduced partition function ratios, which in turn can be used to calculate inter-mineral isotope fractionation factors, seem to be ubiquitous in all minerals. The ionic radius difference of two cations, K and Na in feldspars and Ca and Mg in orthopyroxene and carbonate minerals, also plays a critical role controlling their corresponding reduced partition function ratios. Because of the similar crystal structures and K (Na)-O bonding environments of low and high temperature phases of alkali feldspars, our calculations on the low temperature microcline-low albite series can be applied to the

high temperature solution series, including the orthoclase-high albite and sanidine-high albite solution series.

The inter-mineral isotope fractionation factor, $10^3 \ln {}^{41K/39K}\alpha_{feldspar-microcline}$, between alkali feldspar with a $K/(K + Na)$ of 1/16 and microcline is 2.21‰ at 300 K, and 0.42‰ at 700 K. The lowest $K/(K + Na)$ explored in our study is 1/16, and low albites found in natural rocks typically have $K/(K + Na)$ less than 1/16 (Harlow and Brown, 1980; Smith and Brown, 1988; Armbruster et al., 1990; Fedo et al., 1997; Spötl et al., 1999; Zhou et al., 2013). Thus larger $10^3 \ln {}^{41K/39K}\alpha_{feldspar-microcline}$ is expected for natural albites. Plagioclase, a solid solution series of albite and anorthite, is probably enriched in heavy K isotopes relative to alkali felspars because of its low $K/(K + Na + Ca)$. The size of K isotope fractionation among low albite, anorthite and microcline caused by concentration effect is comparable to the K isotope variation observed in both terrestrial and extraterrestrial samples. The concentration effects on K isotopes must be taken into account in future K isotope study.

ACKNOWLEDGEMENTS

APPENDIX A. SUPPLEMENTARY MATERIAL

Supplementary data associated with this article can be found, in the online version, at https://doi.org/10.1016/j.gca.2018.11.006.

REFERENCES

Anderson R. S. and Anderson S. P. (2010) Geomorphology: The Mechanics and Chemistry of Landscapes. Cambridge University Press, The Edinburgh Building, Cambridge CB2 8RU, UK.

Angel R. J., Ross N. L., Zhao J., Sochalski-Kolbus L., Kruger H. and Schmidt B. C. (2013) Structural controls on the anisotropy of tetrahedral frameworks: the example of monoclinic feldspars. *Eur. J. Mineral.* **25**, 597–614.

Armbruster T., Burgi H., Kunz M., Gnos E., Bronnimann S. and Lienert C. (1990) Variation of displacement parameters in structure refinements of low albite. *Am. Mineral.* **75**, 135–140.

Blasi A., Blasi C. D. P. and Zanazzi P. F. (1987) A re-examination of the pellotsalo microcline: mineralogical implicanons and genetic consideration. *Can. Mineral.* **25**, 527–537.

Bloom H. E., Chen H., Fegley B., Lodders K. and Wang K. (2018) Potassium isotope compositions of carbonaceous and ordinary chondrites: implications on the origin of volatile depletion in the early solar system. *49th Lunar and Planetary Science Conference, The Woodlands, Texas*, p. 1193.

Chao S. H., Hargreaves A. and Taylor W. H. (1940) The structure of orthoclase. *Mineral. Mag.* **25**, 498–512.

Chauvel C. and Hémond C. (2000) Melting of a complete section of recycled oceanic crust: Trace element and Pb isotopic evidence from Iceland. *Geochem. Geophy. Geosy.* **1**, 1001.

Chen H., Meshik A. P., Pravdivtseva O. V., Day J. M. D. and Wang K. (2018a) Evaporative fractionation of potassium isotopes during the first nuclear detonation and implication on the formation of the Moon. *49th Lunar and Planetary Science Conference, The Woodlands, Texas*, p. 1193.

Chen H., Liu X.-M. and Wang K. (2018b) Potassium isotopic fractionation during continental weathering. *Goldschmidt Conference*.

Colvilie A. A. (1968) the crystal structure of an adularia and a refinement of the structure of orthoclase. *Am. Mineral.* **53**, 25–37.

Couty R. and Velde B. (1986) Pressure-induced band splitting in infrared spectra of sanidine and albite. *Am. Mineral.* **71**, 99–104.

Dal Corso A., Baroni S., Resta R. and de Gironcoli S. (1993) Ab initio calculation of phonon dispersions in II–VI semiconductors. *Phys. Rev. B* **47**, 3588–3592.

Downs R. T., Andalman A. and Hudacsko M. (1996) The coordination numbers of Na and K atoms in low albite and microcline as determined from a procrystal electron-density distribution. *Am. Mineral.* **81**, 1344–1349.

Downs R. T., Hazen R. M. and Finger L. W. (1994) The high-pressure crystal chemistry of low albite and the origin of the pressure dependency of Al-Si ordering. *Am. Mineral.* **79**, 1042–1052.

Fedo C. M., Young G. M., Nesbitt H. W. and Hanchar J. M. (1997) Potassic and sodic metasomatism in the Southern Province of the Canadian Shield: evidence from the Paleoproterozoic Serpent Formation, Huronian Supergroup, Canada. *Precambrian Res.* **84**, 17–36.

Feng C., Qin T., Huang S., Wu Z. and Huang F. (2014) First-principles investigations of equilibrium calcium isotope fractionation between clinopyroxene and Ca-doped orthopyroxene. *Geochim. Cosmochim. Acta* **143**, 132–142.

Frey F. A., Huang S., Xu G. and Jochum K. P. (2016) The Geochemical components that distinguish Loa- and Kea-Trend Hawaiian shield lavas. *Geochim. Cosmochim. Acta* **185**, 160–181.

Gazel E., Hayes J. L., Hoernle K., Kelemen P., Everson E., Holbrook W. S., Hauff F., Bogaard P. V. D., Vance E. A. and Chu S. Y. (2015) Continental crust generated in oceanic arcs. *Nat. Geosci.* **8**, 321–327.

Giannozzi P., Baroni S., Bonini N., Calandra M., Car R., Cavazzoni C., Ceresoli D., Chiarotti G. L., Cococcioni M., Dabo I., Dal Corso A., de Gironcoli S., Fabris S., Fratesi G., Gebauer R., Gerstmann U., Gougoussis C., Kokalj A., Lazzeri M., Martin-Samos L., Marzari N., Mauri F., Mazzarello R., Paolini S., Pasquarello A., Paulatto L., Sbraccia C., Scandolo S., Sclauzero G., Seitsonen A. P., Smogunov A., Umari P. and Wentzcovitch R. M. (2009) QUANTUM ESPRESSO: a modular and open-source software project for quantum simulations of materials. *J. Phys. Condens. Matter* **21**, 395502.

Handke M. and Mozgawa W. (1993) Vibrational spectroscopy of the amorphous silicates. *Vib. Spectrosc.* **5**, 75–84.

Harlow G. and Brown, Jr., G. (1980) Low albite an X-ray and neutron diffraction study. *Am. Mineral.* **65**, 986–995.

Hofmann A. W. and Jochum K. P. (1996) Source characteristics derived from very incompatible trace elements in Mauna Loa and Mauna Kea basalts, Hawaii Scientific Drilling Project. *J. Geophys. Res. Solid Earth* **101**, 11831–11839.

Hu Y., Wu Z., Dera P. K. and Bina C. R. (2016) Thermodynamic and elastic properties of pyrope at high pressure and high

temperature by first- principles calculations. *J. Geophys. Res. Solid Earth* **121**, 6462–6476.

Hu Y., Chen X. Y., Xu Y. K. and Teng F. Z. (2018) High-precision analysis of potassium isotopes by HR-MC-ICPMS. *Chem. Geol.* **493**, 100–108.

Huang F. and Humayun M. (2016) Petrogenesis of high-CaO lavas from Mauna Kea, Hawaii: Constraints from trace element abundances. *Geochim. Cosmochim. Acta* **185**, 198–215.

Huang F., Chen L., Wu Z. and Wang W. (2013) First-principles calculations of equilibrium Mg isotope fractionations between garnet, clinopyroxene, orthopyroxene, and olivine: implications for Mg isotope thermometry. *Earth Planet. Sci. Lett.* **367**, 61–70.

Huang F., Wu Z., Huang S. and Wu F. (2014) First-principles calculations of equilibrium silicon isotope fractionation among mantle minerals. *Geochim. Cosmochim. Acta* **140**, 509–520.

Humayun M. A. A. and Koeberl C. (2004) Potassium isotopic composition of Australasian tektites. *Meteorit. Planet. Sci.* **39**, 1509–1516.

Humayun M. and Cassen P. (2000) Processes determining the volatile abundances of the meteorites and terrestrial planets. In *Origin of the Earth and Moon* (eds. R. M. Canup and K. Righter). University of Arizona Press, Tucson, pp. 3–23.

Humayun M. and Clayton R. (1995a) Precise determination of the isotopic composition of potassium: Application to terrestrial rocks and lunar soils. *Geochim. Cosmochim. Acta* **59**, 2115–2130.

Humayun M. and Clayton R. (1995b) Potassium isotope cosmochemistry: genetic implications of volatile element depletion. *Geochim. Cosmochim. Acta* **59**, 2131–2148.

Jagoutz O. and Behn M. D. (2013) Foundering of lower arc crust as an explanation for the origin of the continental Moho. *Nature* **504**, 131–134.

Jiang Y., Chen H., Fegley B. J., Lodders K., Hsu W., Jacobsen S. B. and Wang K. (2018) High-precision K isotopes of tektites. *In 49th Lunar and Planetary Science Conference, The Woodlands, Texas*.

Keefer K. and Brown G. (1978) Crystal structures and compositions of sanidine and high albite in cryptoperthitic intergrowth. *Am. Mineral.* **63**, 1264–1273.

Kelemen P. B. and Behn M. K. (2016) Formation of lower continental crust by relamination of buoyant arc lavas and plutons. *Nat. Geosci.* **9**, 197–205.

Lee M. R. and Parsons I. (1995) Microtextural controls of weathering of perthitic alkali feldspars. *Geochim. Cosmochim. Acta* **59**, 4465–4488.

Lee M. R., Waldron K. A. and Parsons I. (1995) Exsolution and alteration microtextures in alkali feldspar phenocrysts from the Shap granite. *Mineral. Mag.* **59**, 63–78.

Lee H. L., Peucker-Ehrenbrink B., Chen H., Hasenmueller E. A. and Wang K. (2018) Potassium isotopes in major world rivers: implications for weathering and seawater budget. *Goldschmidt Abstracts*.

Li W., Beard B. and Li S. (2016) Precise measurement of stable potassium isotope ratios using a single focusing collision cell multi-collector ICP-MS. *J. Anal. At. Spectrom.* **31**, 1023–1029.

Lodders K. (2003) Solar System abundances and condensation temperatures of the elements. *Astrophys. J.* **591**, 1220–1247.

Makreski P., Jovanovski G. and Kaitner B. (2009) Minerals from Macedonia. XXIV. Spectra-structure characterization of tectosilicates. *J. Mol. Struct.* **924–926**, 413–419.

McKeown D. A. (2005) Raman spectroscopy and vibrational analyses of albite: From 25 °C through the melting temperature. *Am. Mineral.* **90**, 1506–1517.

Méheut M., Lazzeri M., Balan E. and Mauri F. (2009) Structural control over equilibrium silicon and oxygen isotopic fractionation: a first-principles density-functional theory study. *Chem. Geol.* **258**, 28–37.

Meneghinello E., Alberti A. and Cruciani G. (1999) Order-disorder process in the tetrahedral sites of albite. *Am. Mineral.* **84**, 1144–1151.

Moenke H. (1962) Mineralspektren. I. Akademie-Verlag Press, Berlin.

Morgan L. E., Santiago Ramos D. P., Lloyd N. S. and Higgins J. A. (2018) High precision ^{41}K/^{39}K measurements by MCICP-MS indicate terrestrial variability of δ^{41}K. *J. Anal. Atom. Spectrom.* **33**, 175–186.

Norberg N., Neusser G., Wirth R. and Harlov D. (2011) Microstructural evolution during experimental albitization of K-rich alkali feldspar. *Contrib. Mineral. Petrol.* **162**, 531–546.

Orvilie P. M. (1967) Unit-cell parameters of the microcline-low albite and the sanidine-high albite solid solution series. *Am. Mineral.* **52**, 55–86.

Parendo C. A., Jacobsen S. B. and Wang K. (2017) K isotopes as a tracer of seafloor hydrothermal alteration. *Proc. Natl. Acad. Sci. USA* **114**, 1827–1831.

Parsons I. (1978) Feldspars and fluids in cooling plutons. *Miner. Mag.* **42**, 1–17.

Parsons I. (2010) Feldspars defined and described: a pair of posters published by the Mineralogical Society Sources and supporting information. *Mineral. Mag.* **74**, 529–551.

Parsons I. and Lee M. R. (2009) Mutual replacement reactions in alkali feldspars I: Microtextures and mechanisms. *Contrib. Mineral. Petrol.* **157**, 641–661.

Parsons I., Fitz Gerald J. D. and Martin M. R. (2015) Routine characterization and interpretation of complex alkali feldspar intergrowths. *Am. Mineral.* **100**, 1277–1303.

Perdew J. P. and Zunger A. (1981) Self-interaction correction to density-functional approximations for many-electron systems. *Phys. Rev. B* **23**, 5048–5079.

Peterson M. E., Saal A. E., Nakamura E., Kitagawa H., Kurz M. D. and Koleszar A. M. (2014) Origin of the "Ghost Plagioclase" signature in galapagos melt inclusions: new evidence from Pb isotopes. *J. Petrol.* **55**, 2193–2216.

Phillips M. W. and Ribbe P. H. (1973) The structures of monoclinic potassium-rich feldspars. *Am. Mineral.* **58**, 263–270.

Powell M. and Powell R. (1977) Plagioclase-alkali feldspar geothermometry revisited. *Mineral. Mag.* **4**, 253–256.

Prewitt C. T., Sueno S. and Papike J. J. (1976) The crystal structures of high albite and monalbite at high temperature. *Am. Mineral.* **61**, 1213–1225.

Qin T., Wu F., Wu Z. and Huang F. (2016) First-principles calculations of equilibrium fractionation of O and Si isotopes in quartz, albite, anorthite, and zircon. *Contrib. Mineral. Petrol.* **171**, 91.

Richter F. M., Mendybaev R. A., Christensen J. N., Ebel D. and Gaffney A. (2011) Laboratory experiments bearing on the origin and evolution of olivine-rich chondrules. *Meteorit. Planet. Sci.* **46**, 1152–1178.

Saal A. E., Bourdon B., Kurz M. D., Hauri E. H. and Sims K. W. (2007) Temperature versus buoyant mantle heterogeneities, evaluating the origin of OIB using the galapagos archipelago. *Eos Trans. AGU, Fall Meet. Suppl., Abstract.*, V42B-05.

Santiago Ramos D. P., Morgan L. E., Lloyd N. S. and Higgins J. A. (2018) Reverse weathering in marine sediments and the geochemical cycle of potassium in seawater: insights from the K isotopic composition (^{41}K/^{39}K) of deep-sea pore-fluids. *Geochim. Cosmochim. Acta.* https://doi.org/10.1016/j.gca.2018.02.035 (available online 2 March 2018).

Schauble E., Rossman G. R. and Taylor H. P. (2004) Theoretical estimates of equilibrium chromium-isotope fractionations. *Chem. Geol.* **205**, 99–114.

Shannon R. D. (1976) Revised effective ionic radii and systematic studies of interatomic distances in halides and chalcogenides. *Acta Crystallogr. A* **32**, 751–767.

Sharma S. K., Misra A. K., Clegg S. M., Barefield J. E., Wiens R. C. and Acosta T. (2010) Time-resolved remote Raman study of minerals under supercritical CO_2 and high temperatures relevant to Venus exploration. *Philos. Trans. R. Soc. A* **368**, 3167–3191.

Smith J. V. and Brown W. L. (1988) Feldspar Minerals Volume 1 Crystal Structures, Physical, Chemical, and Microtextural Properties, Second received and extended edition. Springer-Verlag Press, Heidelberg.

Sobolev A. V., Hofmann A. W. and Nikogosian I. K. (2000) Recycled oceanic crust observed in "ghost plagioclase" within the source of Mauna Loa lavas. *Nature* **404**, 986–990.

Spötl C., Longstaffe F. J., Ramseyer K. and Rüdinger B. (1999) Authigenic albite in carbonate rocks – a tracer for deep-burial brine migration? *Sedimentology* **46**, 649–666.

Tamura Y., Sato T., Fujiwara T., Kodaira S. and Nichols A. (2016) Advent of continents: a new hypothesis. *Sci. Rep.* **6**, 33517.

Tian Z., Chen H., Fegley, Jr., B., Lodders K., Barrat J.-A. and Wang K. (2018a) Potassium isotope differences among chondrites, earth, moon, mars, and 4-vesta – implication on the planet accretion mechanisms. *Lunar Planet. Sci. Conf.* **49**, 1276.

Tian Z., Chen H., Fegley B. J., Lodders K., Korotev R. L. and Wang K. (2018b) Potassium isotopic composition of the moon. *Goldschmidt Abstracts*.

Troullier N. and Martins J. L. (1991) Efficient pseudopotentials for plane-wave calculations. 2. Operators for fast iterative diagonalization. *Phys. Rev. B* **43**, 8861–8869.

Tseng H. Y., Heaney P. J. and Onstott T. C. (1995) Characterization of lattice strain-induced by neutron-irradiation. *Phys. Chem. Miner.* **22**, 399–405.

Tuller-Ross B., Lee H. L., Chen H., Marty B., Kelley K. A. and Wang K. (2018) Potassium isotopic systematics of oceanic basalts. *Goldschmidt Abstracts*.

Urey H. C. (1947) The thermodynamic properties of isotopic substances. *J. Chem. Soc. (Lond.)*, 562–581.

Vanderbilt D. (1990) Soft self-consistent pseudopotentials in a generalized eigenvalue formalism. *Phys. Rev. B* **41**, 7892.

Velde B. and Boyer H. (1985) Raman microprobe spectra of naturally shocked microcline feldspar. *J. Geophys. Res.* **99**, 3675–3682.

Velde B., Syono Y., Kikuchi M. and Boyer H. (1989) Raman microprobe study of synthetic diaplectic plagioclase feldspars. *Phys. Chem. Miner.* **16**, 436–441.

Villar S. E. J. and Edwards H. G. M. (2005) Near-infrared Raman spectra of terrestrial minerals: relevance for the remote analysis of Martian spectral signatures. *Vib. Spectrosc.* **39**, 88–94.

Waldron K. A., Parsons I. and Brown W. L. (1993) Solution-redeposition and the orthoclase-microcline transformation: evidence from granulites and relevance to ^{18}O exchange. *Mineral. Mag.* **57**, 687–695.

Wang K. and Jacobsen S. B. (2016a) An estimate of the bulk silicate earth potassium isotopic composition based on MC-ICPMS measurements of basalts. *Geochim. Cosmochim. Acta* **178**, 223–232.

Wang K. and Jacobsen S. B. (2016b) Potassium isotopic evidence for a high-energy giant impact origin of the Moon. *Nature* **538**, 487–490.

Wang W., Qin T., Zhou C., Huang S., Wu Z. and Huang F. (2017a) Concentration effect on equilibrium fractionation of Mg-Ca isotopes in carbonate minerals: insights from first-principles calculations. *Geochim. Cosmochim. Acta* **208**, 185–197.

Wang W., Zhou C., Qin T., Kang J., Huang S., Wu Z. and Huang F. (2017b) Effect of Ca content on equilibrium Ca isotope fractionation between orthopyroxene and clinopyroxene. *Geochim. Cosmochim. Acta* **219**, 44–56.

Wentzcovitch R. M. (1991) Invariant molecular-dynamics approach to structural phase transitions. *Phys. Rev. B* **44**, 2358–2361.

White J. C., Holt G. S., Parker D. F. and Ren M. (2003) Rencrystallization: the Leyva Canyon volcano, Trans-Pecos magmatic province, Texas. *J. Volcanol. Geoth. Res.* **111**, 155–182.

Wu Z., Huang F. and Huang S. (2015) Isotope fractionation induced by phase transformation: first-principles investigation for Mg_2SiO_4. *Earth Planet. Sci. Lett.* **409**, 339–347.

Yang H.-J., Frey F. A. and Clague D. A. (2003) Constraints on the source components of lavas forming the Hawaiian north arch and Honolulu volcanics. *J. Petrol.* **44**(4), 603–627.

Yu Y., Hewins R. H. and Wang J. (2003) Experimental study of evaporation and isotopic mass fractionation of potassium in silicate melts. *Geochim Cosmochim. Acta* **67**, 773–786.

Zeng H., Dauphas N., Meheut M., Blanchard M. and Galli G. (2018) First-principle computations of equilibrium potassium isotopic fractionation in orthoclase. *Lunar Planet. Sci. Conf.* **49**, 2452.

Zhou Q. F., Qin K. Z., Tang D. M., Ding J. G. and Guo Z. L. (2013) Mineralogy and significance of micas and feldspars from the Koktokay No. 3 pegmatitic rare-element deposit, Altai. *Acta Petrol. Sin.* **29**, 3004–3022 (in Chinese with English abstract).

Associate editor: Frederic Moynier